



PCCP

**Vibrational energy redistribution during donor-acceptor
electronic energy transfer: criteria to identify subsets of
active normal modes**

Journal:	<i>Physical Chemistry Chemical Physics</i>
Manuscript ID	CP-ART-06-2020-003102.R1
Article Type:	Paper
Date Submitted by the Author:	24-Jul-2020
Complete List of Authors:	Alfonso-Hernandez, Laura; CONICET - Centro Atómico Bariloche, Centro Integral de Medicina Nuclear y Radioterapia ATHANASOPOULOS, Stavros; Universidad Carlos III de Madrid, Departamento de Física Tretiak, Sergei; Los Alamos National Laboratory, Theoretical Division Miguel, Beatriz; Universidad Politécnica de Cartagena, Ingeniería Química y Ambiental Bastida, Adolfo; Universidad de Murcia, Química Física Fernandez-Alberti, Sebastian; Universidad Nacional de Quilmes, Ciencia y Tecnología

SCHOLARONE™
Manuscripts

Vibrational energy redistribution during donor-acceptor electronic energy transfer: criteria to identify subsets of active normal modes

L. Alfonso-Hernandez¹, S. Athanasopoulos², S. Tretiak³, B. Miguel⁴, A. Bastida⁵, and S. Fernandez-Alberti⁶.

¹CONICET - Centro Integral de Medicina Nuclear y Radioterapia, Centro Atómico Bariloche, Av. Bustillo 9500, S. C. de Bariloche, Río Negro, 8400 Argentina

²Departamento de Física, Universidad Carlos III de Madrid, Avenida Universidad 30, 28911 Leganés, Madrid, Spain.

³Theoretical Division, Center for Nonlinear Studies (CNLS), and Center for Integrated Nanotechnologies (CINT), Los Alamos National Laboratory, Los Alamos, NM 87545, USA.

⁴Departamento de Ingeniería Química y Ambiental, Universidad Politécnica de Cartagena, 30203 Cartagena, Spain

⁵Departamento de Química Física, Universidad de Murcia, 30100 Murcia, Spain.

⁶Departamento de Ciencia y Tecnología, Universidad Nacional de Quilmes/CONICET, B1876BXD Bernal, Argentina

ABSTRACT

Photoinduced electronic energy transfer in conjugated donor-acceptor systems is naturally accompanied by intramolecular vibrational energy redistributions accepting an excess of electronic energy. Herein, we simulate these processes in a covalently linked donor-acceptor molecular dyad system by using nonadiabatic excited state molecular dynamics simulations. We analyze different complementary criteria to systematically identify the subset of vibrational normal modes that actively participate on the donor→acceptor ($S_2 \rightarrow S_1$) electronic relaxation. We analyze energy transfer coordinates in terms of state-specific normal modes defined according to the different potential energy surfaces (PESs) involved. On one hand, we identify those vibrations that contribute the most to the direction of the main driving force on the nuclei during electronic transitions, represented by the non-adiabatic derivative coupling vector between donor and acceptor electronic states. On the other hand, we monitor normal mode transient accumulations of excess energy and their intramolecular energy redistribution fluxes. We observe that the subset of active modes varies according to the PES on which they belong and these modes experience the most significant rearrangements and mixing. Whereas the nuclear motions that promote donor→acceptor energy funneling can be localized mainly on one or two normal modes of the S_2 state, they become spread out across multiple normal modes of the S_1 state following the energy transfer event.

I. INTRODUCTION

Currently, there is a strong interest in understanding the dynamic behaviour of photoexcitations in multichromophoric systems such as molecular wires¹, conjugated polymers², solid state molecular assemblies^{3,4,5}, and macrocycles⁶, with an ultimate goal to control and direct energy transfer for catering a system specific functionality. Technological driven examples include among others light harvesting⁷, photoconversion^{8,9}, light emission, fluorescent imaging and sensing. In principle, electronic energy transfer between donor and acceptor chromophoric units is uniquely marked by an accompanying vibrational energy redistribution. The identification of vibrations that actively participate in the donor→acceptor electronic energy transfer by coupling the excited states localized on donor/acceptor moieties, represent a valuable footprint of the process and a possible mean to manipulate the efficiency of energy dissipation in novel optical-electronic devices^{10,11,12,13,14}. We refer to these nuclei motions as “active” vibrational modes.

Experimental techniques based on excited-state IR spectroscopy^{15,16,17} can be applied to assign and identify structural changes and photochemical pathways in excited state dynamics. Furthermore, ultrafast time-resolved transient IR and Raman spectroscopy^{18,19,20,21,22,23,24,25,26,27,28,29,30,31,32,33,34} allow the evaluation of vibrational energy relaxation rates in a large variety of organic compounds^{18,19,20,21,22,24,26, 27,28,30, 35}, providing details for the flow of intramolecular vibrational energy. These techniques can in principle quantify the instantaneous populations of participating molecular vibrations in real time. The analysis of experimental measurements is usually performed in terms of vibrational band assignment using the standard equilibrium normal modes (ENM)^{36,37,38,39}. The ENMs are typically calculated from the second derivatives of the ground-state (GS) energy with respect to nuclear coordinates (i.e., the Hessian matrix)⁴⁰. However, photoinduced processes, that take place after UV-visible photoexcitation of organic conjugated molecules with donor and acceptor chromophoric units, involve several coupled electronic excited states. Internal conversion often results from a passage through unavoided crossings^{41,42} leading to electronic population exchanges between these states. As a consequence, the vibrational normal mode identities in multichromophoric conjugated molecules are generally not preserved during electronic dynamics⁴³. Unavoided crossings may introduce a reordering and/or transient mixing, which changes the adiabatic electronic state identities and causes vibrational normal modes to become mixed in regions of strong non-adiabatic coupling. Henceforth, the one-to-one correspondence between normal modes of two radiatively or non-radiatively coupled electronic states can be lost⁴⁴. The above normal mode mixing, known as the Dushinsky effect⁴³, breaks the mirror-image symmetry between the emission and absorption spectra corresponding to a given electronic transition^{45,46} and it affects the IR/Raman excitation profiles of the mixed modes^{47,48,49,50}.

Intramolecular vibrational energy transfer in organic molecules is commonly simulated with effective Hamiltonians by applying harmonic approximations to identify the pathways and lifetimes of a specific mode or bond energy relaxation^{51,52,53}. For example, using a parametrized Hamiltonian describing the coupling between a set of discrete electronic states with a set of phonon oscillators in combination with golden-rule transfer rates, Bittner et al were able to identify active electron transfer vibrational coordinates in donor-acceptor systems^{54,55,56,57,58}. Vibrational energy relaxation and redistribution can be monitored following the evolution in time of the kinetic energy of each ENM. Atomistic simulation of simultaneous nonadiabatic

excited-state electronic and vibrational energy relaxation and redistribution in donor-acceptor systems requires an analysis in terms of state-specific normal modes defined according to the respective potential energy surfaces (PESs) involved. Excited-state equilibrium normal modes (ES-ENMs) can be obtained from the excited-state PES. Despite the presence of anharmonicities and mode couplings, ES-ENMs offer a straightforward way of examining experimental vibronic spectra by providing, up to a level of approximation, decoupled directions of motion associated with the shape of the corresponding PESs.

In a previous publication, we reported an ultrafast donor→acceptor intramolecular electronic energy transfer in the molecular dyad system comprising a ladder-type poly(para-phenylene) oligomer donor unit (LPPP5) covalently linked with a perylenemonoimide acceptor unit (PMI) (see **Figure 1a**)^{59,54}. In this contribution, we shall characterize the role of vibrational energy redistribution during the internal conversion process of the model LPPP5-PMI dyad system using atomistic non-adiabatic excited-state molecular dynamics (NEXMD) simulations. In this way, LPPP5-PMI dyad is used as a model system to analyze different criteria to systematically identify and characterize the subset of active normal modes from atomistic non-adiabatic excited state molecular dynamics simulations. We distinguish these active nuclei motions from vibrations that serve as a bath of coupled harmonic oscillators to which the excess of energy, transiently accumulated in the active modes, is subsequently transferred.

II. METHODS

A. The NEXMD framework

The NEXMD^{60,61} computational package allows the simulation of the photoexcitation and subsequent nonadiabatic electronic and vibrational energy relaxation and redistribution in large multichromophoric conjugated molecules, a process that involves several coupled electronic excited states. The code is based on the implementation of the fewest switches surface hopping (FSSH) algorithm^{62,63} with specific treatments of decoherence⁶⁴ and trivial unavoided crossings⁴². Excited-state energies^{65,66,67}, gradients^{68,69}, and non-adiabatic coupling terms^{61,70,71,72} are calculated “on the fly” using the Collective Electronic Oscillator (CEO) approach^{73,74,75} at the configuration interaction singles (CIS) level using the semiempirical AM1 Hamiltonian⁷⁶. While nuclei are propagated classically the electronic wave function $\psi(\mathbf{r}, \mathbf{R}, t)$ is propagated quantum-mechanically on the basis of adiabatic CIS electronic states $\phi_\alpha(\mathbf{r}; \mathbf{R})$:

$$M_i \ddot{\mathbf{R}}_i = -\nabla_{\mathbf{R}} E_\alpha(\mathbf{R}) \quad (1)$$

$$\psi(\mathbf{r}, \mathbf{R}, t) = \sum_\alpha c_\alpha(t) \phi_\alpha(\mathbf{r}; \mathbf{R}) \quad (2)$$

$$i\hbar \dot{c}_\alpha(t) = c_\alpha(t) E_\alpha(\mathbf{R}) - i\hbar \sum_\beta c_\beta(t) \dot{\mathbf{R}} \cdot \mathbf{d}_{\alpha\beta} \quad (3)$$

Here M_i , \mathbf{R} , $\dot{\mathbf{R}}$ and $\ddot{\mathbf{R}}_i$ are the mass, position, velocity and acceleration of the i^{th} nuclei, respectively, $E_\alpha(\mathbf{R})$ is the energy of the α^{th} electronic excited state, \mathbf{r} are the electronic coordinates, and $\mathbf{d}_{\alpha\beta}$ are the non-adiabatic derivative coupling vectors (NACR _{$\alpha\beta$}) defined as

$$\mathbf{d}_{\alpha\beta} = \langle \phi_\alpha(\mathbf{r}; \mathbf{R}) | \nabla_{\mathbf{R}} \phi_\beta(\mathbf{r}; \mathbf{R}) \rangle \quad (4)$$

Within the NEXMD framework, the spatial extent of excitonic wavefunction is analyzed in terms of the transition density matrices $(\rho^{g\alpha})_{nm} \equiv \langle \phi_\alpha(\mathbf{r}; \mathbf{R}(t)) | c_m^\dagger c_n | \phi_g(\mathbf{r}; \mathbf{R}(t)) \rangle$ (denoted *electronic normal modes*)^{77,78}. c_m^\dagger (c_n) are the creation (annihilation) electronic operator; and indices n and m refer to atomic orbital (AO) basis functions. Diagonal elements $(\rho^{g\alpha})_{nn}$ are relevant to the changes in the distribution of electronic density induced by photoexcitation from the ground state g to an excited electronic state α ⁷⁹. The fraction of the transition density localized on each chromophore segment, that is, donor and acceptor units (see **Figure 1(a)**), is evaluated as

$$\delta_X^\alpha(t) = (\rho^{g\alpha}(t))_X^2 = \sum_{n_A, m_A} (\rho^{g\alpha}(t))_{n_A m_A}^2 \quad (5)$$

where the index A runs over all atoms localized on the X chromophore unit ($X = \text{donor, acceptor}$).

More details about the NEXMD approach, implementation, and testing parameters can be found elsewhere^{60,61,80}.

B. Normal Mode Analysis

Ground-state and Excited-state equilibrium normal modes (ES-ENM(S_α), $\alpha=0,1,2$) analysis has been performed at each corresponding equilibrium structure \mathbf{R}_0^α obtained after performing geometry optimization of the molecular system on the corresponding S_α PES. Geometry optimizations are completed using the NEXMD with the AM1 Hamiltonian⁷⁶. Each final optimized structure is translated and rotated to a *body-fixed* Cartesian reference frame with origin in its center of mass and its inertial axis coincident with the Cartesian x, y, z axis.

ENM(S_α) are computed from the mass-weighted Hessian matrix \mathbf{H} with elements

$$H_{ij}^\alpha(\mathbf{R}_0^\alpha) = -\partial^2 E_\alpha / \partial q_i \partial q_j |_{\mathbf{R}_0^\alpha} \quad (6)$$

where E_α is the potential energy of S_α state and $q_{3i-2}^\alpha = \sqrt{M_i}(X_i - X_{0,i}^\alpha)$, $q_{3i-1}^\alpha = \sqrt{M_i}(Y_i - Y_{0,i}^\alpha)$ and $q_{3i}^\alpha = \sqrt{M_i}(Z_i - Z_{0,i}^\alpha)$ are the mass weighted Cartesian displacements of the i^{th} atom with equilibrium coordinate $\mathbf{R}_{0,i}^\alpha = (X_{0,i}^\alpha, Y_{0,i}^\alpha, Z_{0,i}^\alpha)$ defined in a body-fixed reference frame with the origin at the center of mass of the molecule and axes corresponding to its principle axes of inertia. ENMs ($\{\mathbf{Q}_i^\alpha\}$, ($i=1, \dots, 3N-6$), where N is the number of atoms in the molecule), and their frequencies ($\nu_i^\alpha = (\sqrt{\lambda_i^\alpha}/2\pi)$) are then obtained upon diagonalization of \mathbf{H}^α from the corresponding eigenvector matrix \mathbf{L}^α and its eigenvalues. Excited-state ENM are computed in the locally diabatic representation, see Ref.⁸¹.

The ENM(S_α) amplitudes are obtained throughout the NEXMD simulations as a linear combination of the set $\{\mathbf{q}_i^\alpha\}$, ($i=1, \dots, 3N$) as

$$\mathbf{Q}_i^\alpha(t) = \sum_{j=1}^{3N} l_{ji}^\alpha \mathbf{q}_j^\alpha(t) \quad i=1, \dots, 3N-6 \quad (7)$$

where l_{ji}^α are the elements of a matrix \mathbf{L}^α . In the same way, the ENM momenta are obtained as

$$\dot{\mathbf{Q}}_i^\alpha(t) = \sum_{j=1}^{3N} l_{ji}^\alpha \dot{\mathbf{q}}_j^\alpha(t) \quad i=1, \dots, 3N-6 \quad (8)$$

At this point it is important to stress that our NEXMD simulations are performed in the *space-fixed* Cartesian coordinates. Matrix \mathbf{L}^α is the linear transformation matrix that express the set of $\{\mathbf{Q}_i^\alpha\}$ on the basis of mass-weighted Cartesian displacements $\{\mathbf{q}_j^\alpha\}$ defined in the *body-fixed* Cartesian reference frame with the origin in its center of mass and its inertial axis coincident with the original Cartesian x,y,z axis. Therefore, in order to apply eqs. (7-8), coordinates and velocities obtained from the NEXMD simulations must be erstwhile translated and rotated from the *space-fixed* to the *body-fixed* reference frame.

Subsequently, vibrational kinetic energy is calculated by summing up the contribution of each ENM as

$$K(t) = \sum_{j=1}^{3N-6} K_i(t) = \frac{1}{2} \sum_{j=1}^{3N-6} (\dot{\mathbf{Q}}_i^\alpha(t))^2 \quad (9)$$

and the total vibrational energy associated with a given ENM is obtained from the virial theorem, $E_i(t) = 2K_i(t)$.

Molecular fluctuations at room temperature lead to structural distortions spanning regions of the phase space which are far away from the equilibrium geometry, \mathbf{R}_0^α , at which the ENMs have been calculated. Particularly, the presence of flexible dihedral angles connecting different moieties and/or chromophoric units introduces changes in the relative orientation between the units. This may hinder the identification of the contribution of the different nuclear Cartesian coordinates to each individual ENM velocity (see eq. 8). In order to resolve this issue, we make use of the Rodrigues' rotation formula that is an algorithm for rotating a vector in space, given an axis and angle of rotation. In the present work, we apply the formula to rotate the velocities of atoms that belong to the PMI acceptor around the dihedral angle θ that connects it with the LPPP5 donor (see **Figure 1(a)**). If we define $\Delta\theta$ as the difference between the values of the dihedral angle θ evaluated at a molecular structure obtained at a given time t during NEXMD simulation and its value at the equilibrium geometry \mathbf{R}_0^α , we can calculate

$$\dot{\mathbf{q}}' = \dot{\mathbf{q}} \cos \Delta\theta + (\mathbf{k} \times \dot{\mathbf{q}}) \sin \Delta\theta + \mathbf{k}(\mathbf{k} \cdot \dot{\mathbf{q}})(1 - \cos \Delta\theta) \quad (10)$$

Here $\dot{\mathbf{q}}$ is the vector containing the momenta of all atoms that belong to PMI acceptor, \mathbf{k} is a unitary vector in the direction of the central bond that define the dihedral angle θ . This way, ENM momenta can be calculated as

$$\dot{\mathbf{Q}}_i^\alpha(t) = \sum_{j \in \text{donor}} l_{ji}^\alpha \dot{\mathbf{q}}_j^\alpha(t) + \sum_{j \in \text{acceptor}} l_{ji}^\alpha \dot{\mathbf{q}}_j'^\alpha(t) \quad (11)$$

Therefore, equation 11 can be used to evaluate the contribution of each ENM to the vibrational kinetic energy (eq. 9).

In the present work, different sets of normal modes have been calculated. That is, ENM(S_α)($\alpha=1,2$), or ENMs evaluated on different minima of the potential energy surfaces. The analysis of the vibrational energy flux requires the *one-by-one* assignment of each normal mode of one set $\{\mathbf{Q}_i\}$ to each normal mode of the other set $\{\mathbf{Q}_j\}$. The correspondence between modes

in both sets is based on the highest values of their overlaps. The maximum overlaps are obtained through the maximization of the trace of the square of the overlap matrix \mathbf{O} whose elements are defined as the dot product

$$O_{ii'} = \mathbf{Q}_i^T \cdot \mathbf{Q}'_{i'} \quad (12)$$

This can be done by selecting those elements of the \mathbf{O} matrix, one for each row, and each pertaining to a different column (or vice versa), which maximize the sum of their squared values. In order to do that, we have used a variant of the Min-Cost algorithm^{82,83}.

C. Non-adiabatic derivative coupling analysis

Comparison of non-adiabatic derivative couplings \mathbf{d}_{12} defined by eq. 4 for the different trajectories is performed as follows: We first construct the matrix \mathbf{A} of dimension $3N \times K$, with K being the number of NEXMD trajectories featuring an effective $S_2 \rightarrow S_1$ transition. We define an effective $S_2 \rightarrow S_1$ transition, or a hop, as the last $S_2 \rightarrow S_1$ transition without further $S_1 \rightarrow S_2$ back-hopping during the rest of the trajectory dynamics. Matrix \mathbf{A} is built with columns representing the \mathbf{d}_{12} at the moment of effective $S_2 \rightarrow S_1$ transition in each of the K NEXMD trajectories. Thereafter, Singular Value Decomposition (SVD) of matrix \mathbf{A} has been performed. That is,

$$\mathbf{A} = \mathbf{U} \cdot \mathbf{W} \cdot \mathbf{V}^T \quad (13)$$

where matrix \mathbf{U} is a $3N \times K$ column-orthogonal matrix, and \mathbf{V} and \mathbf{W} are $K \times K$ diagonal and orthogonal matrices respectively. We denote \mathbf{d}_{12}^{SVD} as the first column of matrix \mathbf{U} with the associated largest value of w_1 .

A further inspection of \mathbf{d}_{12} vectors is performed by projecting it onto the ENM(S_1) and ENM(S_2) basis sets

$$\mathbf{d}_{12} = \sum_{i=1}^{3N-6} c_i^\alpha \mathbf{Q}_i^\alpha \quad (\alpha=1,2) \quad (13)$$

with $c_i^\alpha = \mathbf{d}_{12} \cdot \mathbf{Q}_i^\alpha$. The participation number PN of these projections is given by^{84,85}

$$PN^\alpha = \left(\sum_{i=1}^{3N-6} (c_i^\alpha)^4 \right)^{-1} \quad (14)$$

PN^α represents the number of ENMs(S_α) that contribute to \mathbf{d}_{12} . Values of $PN^\alpha \approx 3N-6$ indicate the fully delocalized \mathbf{d}_{12} with contributions from every ENM(S_α), whereas $PN^\alpha \approx 1$ corresponds to \mathbf{d}_{12} being identical to a unique ENM(S_α).

D. Vibrational energy redistribution pathways

The vibrational energy redistribution pathways during donor-acceptor electronic energy transfer can be identified by using the previously developed Statistical Minimum Flow (SMF)⁸⁶, originally developed to analyze the vibrational energy flow in polyatomic molecules

using Instantaneous Normal Modes(INM). Herein, we applied it in terms of ENM(S_α) and we briefly outline its basic equations below.

During NEXMD simulations, at each time interval Δt , the effective change of total vibrational energy associated with a given ENM, $E_i(t)$ ($\Delta E_i(t)$) is monitored by the flow matrix $F(t)$ with diagonal elements of zero and off-diagonal elements $f_{XY}(t)$ containing the amount of $E_i(t)$ transferred between the X and Y ENMs. We classify ENMs as donors (D) if $\Delta E_i(t) < 0$ or acceptors (A) if $\Delta E_i(t) > 0$. By imposing the minimum flow criterion, that assumes that the amount of $\Delta E_i(t)$ is a minimum, we consider only the effective $E_i(t)$ flows from D to A. The total vibrational energy exchanged among ENMS during Δt is

$$\Delta E_{\text{total}}(t) = \sum_{X \in D} |\Delta E_X(t)| = \sum_{Y \in A} \Delta E_Y(t) \quad (15)$$

And elements $f_{XY}(t)$ are calculated as

$$f_{XY}(t) = -f_{YX}(t) = \begin{cases} - & X \in D, Y \in A \\ 0 & X, Y \in D \text{ or } X, Y \in A \end{cases} \quad (16)$$

A detailed derivation of eqs (15) and (16) can be found elsewhere⁸⁶.

E. Computational details

The NEXMD simulations were performed on the model LPPP5-PMI dyad system at constant energy. 1 ns of an equilibrated ground state molecular dynamics simulation at 300 K with Langevin friction coefficient $\gamma=20.0 \text{ ps}^{-1}$ has been employed to generate the required conformational sampling of initial positions and momenta for the subsequent NEXMD simulations.

Four hundred (400) individual NEXMD trajectories were started from these initial configurations by instantaneously promoting the system to the second excited state S_2 . A classical time step of 0.5 fs has been used for nuclei propagation in ground state dynamics.

A classical time step of 0.1 fs has been used for nuclei propagation and a quantum time step of 0.025 fs has been used to propagate the electronic degrees of freedom for non-adiabatic excited state dynamics modelling. In order to identify and deal with trivial unavoided crossings, we track the state identities using the Min-Cost algorithm as it has been described elsewhere⁸⁷. Moreover, an instantaneous decoherence approach is introduced to account for electronic decoherence⁶⁴, where the electronic wavefunction is collapsed following attempted hop (either successful or forbidden). More details concerning the NEXMD implementation and parameters can be found elsewhere^{88,89,90}.

III. RESULTS AND DISCUSSION

Figure 1(a) depicts the chemical structure of the studied LPPP5(donor)-PMI(acceptor) system and the absorption spectrum, obtained from ground-state equilibrated structures at 300K, is displayed in **Figure 1(b)**. There is a significant overlap between the two lowest excited states

absorption profiles which indicates an interaction between the states. This may affect the initial spatial localization of the exciton after photoexcitation to the S_2 state. Nevertheless, S_1 and S_2 states are mainly spatially localized on different moieties of the dyad, namely, on the donor and the acceptor parts, respectively. This is illustrated in **Figure 1(c)** which shows the localization of the electronic transition densities for S_2 and S_1 at the minimum of the ground state PES.

As we have reported previously⁵⁹, immediately after photoexcitation to the S_2 state, the molecule experiences an ultrafast $S_2 \rightarrow S_1$ internal conversion process (see **Figure 2(a)**) leading to an excitation transfer between donor and acceptor segments. This intramolecular electronic energy redistribution is confirmed by monitoring the time evolution of the fraction of electronic transition density localized on either the donor, $\delta_{\text{donor}}^\alpha(t)$, or the acceptor, $\delta_{\text{acceptor}}^\alpha(t)$ during the $S_2 \rightarrow S_1$ electronic energy relaxation, see **Figure 2(b)**.

In the present work, we are interested in the vibrational energy redistribution during donor-acceptor electronic energy transfer. Our analysis is performed in terms of ES-ENM(S_α), $\alpha=1,2$ that are calculated at the minimum of corresponding PESs. In cases in which the PES presents more than one local minima, the ES-ENM(S_α) calculation is subjected to the ambiguity of the energy minimum selected for their evaluation. This can lead to redefinitions, mixings and reassignment in their frequency ordering. Therefore, we first explore the potential impact of this ambiguity in our analysis. **Figure S1** shows that the PES(S_α) of LPPP5(donor)-PMI(acceptor) present two minima as a function of dihedral angle Φ (see **Figure 1(a)**) between donor and acceptor moieties. The comparisons between the corresponded two sets of ES-ENM(S_α) (i.e. one set per minimum) show that most of the modes remain equivalent and they do not require to be redefined or reassigned in their frequency ordering (see **Figure S2**). Nevertheless, for those normal modes that experience reordering, the reassignments according to the Min-Cost algorithm (see Section II. B) have been taken into account. None of the reassigned modes have been subsequently identified as active mode except for the 227 and 228 ENMs(S_1) that have required switching of their frequency order. Therefore, we found that these reassignments have a minimum effect on our subsequent vibrational analysis of NEXMD simulations.

The values of Φ describe the relative orientations of donor and acceptor moieties. Its distribution in the ground state S_0 across all snapshots is very broad with marginal preferential relative orientations at $\Phi \approx 65^\circ$ and $\Phi \approx 111^\circ$ as shown in the histogram of **Figure 3(a)**. This indicates quite shallow PES for the ground state, where the dihedral angle Φ is well sampled by thermal fluctuations at ambient conditions. The barrier between both conformations is ~ 10.7 meV (**Figure S1**) and the difference between the minima is ~ 3.6 meV, values significantly lower than kT (~ 25.7 meV). After 1ps of excited state dynamics, the values of Φ present a bimodal distribution (see **Figure 3(b)**) that can be adjusted to two Gaussian distributions centered at $\Phi \approx 50^\circ$ and $\Phi \approx 130^\circ$. This bimodal distribution indicates the presence of deeper potential wells in the excited state PES compared to that in the ground state. **Figure S1** confirms that the conformational energy barrier in S_1 state increases to ~ 98.8 meV, indicating that conformational changes are hindered on the excited state. **Figure 3(c)** highlights the formation of these two distributions by the time evolution of Φ during the NEXMD simulations, indicating that the barrier between both conformations is not crossed. Therefore, NEXMD trajectories can be separated in two sets according to their final value of Φ , that is, trajectories with final values of Φ greater or lower than 90° . This result could indicate the presence of two different relaxation pathways with different relaxation rates that lead to these two different final conformations and could require separate treatment. Nevertheless, any attempt to analyze separately both set of trajectories did not reveal any differential dynamics aspect between them

owing to symmetry of the dyad with respect to the dihedral rotation. That is, both sets present equivalent relaxation times and pathways. According to the relative energies of each conformations at the S_1 state (see **Figure S1**), the final equilibrium population of the conformer centered at $\Phi \approx 48^\circ$ is expected to be higher than the population of the conformer centered at $\Phi \approx 120^\circ$. Nevertheless, the approximately equivalent distributions centered at $\Phi \approx 51^\circ$ and $\Phi \approx 130^\circ$, shown in **Figure 3b**, indicate that this is not the case after 1ps after photoexcitation. That is, the final conformational equilibrium should be reached at longer timescales. Despite the significantly lower conformational barrier of ~ 8 meV observed on S_2 state (see **Figure S1**), the ultrafast electronic energy relaxation leads the molecular system on the S_1 state *before* any attempt of conformational population exchange. In what follows we discuss results obtained for the complete set of the NEXMD simulations using ES-ENMs(S_α) calculated at the closest minimum configuration for each trajectory and performing the corresponding reassignments when necessary.

The vibrational energy redistribution concomitant to the electronic energy relaxation after the photoexcitation of LPPP5-PMI can be monitored by evaluating the excess of vibrational energy that transiently accumulates in each normal mode during our NEXMD simulations. This is depicted in **Figure 4** that shows the time dependence of the trajectory averaged vibrational energy ($\langle E_i(t) \rangle$), where i labels normal modes, see eq. 9) of the ENMs for the S_1 and S_2 states. We observe that only a few normal modes, the so-called *active modes*, transiently accumulate an excess of vibrational energy transferred from electronic degrees of freedom during the $S_2 \rightarrow S_1$ internal conversion process. ENMs(S_2), **Figure 4(c)**, transiently localize the excess of energy in less modes than ENMs(S_1), **Figure 4(a)**. The rest of the modes remain with $\langle E_i(t) \rangle$ close to its initial equilibrium value $\approx kT = 0.026$ eV due to the thermostat effect in ground state sampling (**Figure 4(b),(d)**). At this point, it is important to stress that our NEXMD simulations have been performed at constant energy to avoid spurious bath effects at these ultrafast timescales. Therefore, the complete redistribution of the excess electronic energy due to $S_2 \rightarrow S_1$ transition involves two steps. First, the electronic energy is transiently accumulated in a small subset of the active modes within hundreds of femtoseconds. Subsequently, it finally spreads among all $N=300$ vibrational normal modes of the molecule. Most of modes are inactive and seem to act as a bath of coupled harmonic oscillators to which the excess of energy is finally transferred on much longer timescales. The observed final equilibrium values of $\approx kT$, reached by all modes at ~ 1 ps after photoexcitation, indicate that thermal equilibrium is reached faster than the conformational equilibrium discussed previously.

The observed transient accumulation of the excess of energy in a few normal modes can be a consequence of the existence of multiple pathways for donor \rightarrow acceptor electronic and vibrational energy transfer. In order to clarify this issue, we have analyzed the non-adiabatic coupling vectors, \mathbf{d}_{12} , defined in eq. 4. The direction of \mathbf{d}_{12} can be interpreted as the direction of the force on the nuclei during the $S_2 \rightarrow S_1$ transition (the so-called Pechukas force)¹¹. Therefore, the variations among \mathbf{d}_{12} for the different trajectories point to distinct energy transfer pathways. **Figure 5 (a)** shows \mathbf{d}_{12}^{SVD} (defined in Section II.c) and **Figure 5(b)** displays the distribution of the overlap between \mathbf{d}_{12}^{SVD} and the originals \mathbf{d}_{12} corresponding to each NEXMD trajectory. Herein, the first column of matrix \mathbf{U} in eq. 13 is referred as the representative \mathbf{d}_{12}^{SVD} of the whole set. The distribution presents an overlap average value of 0.92. Therefore, all NEXMD trajectories experience the $S_2 \rightarrow S_1$ transition through a common energy transfer pathway in the direction of \mathbf{d}_{12}^{SVD} . The projection of \mathbf{d}_{12}^{SVD} onto the basis of ENMs(S_2) indicates

an overlap of 0.98 between \mathbf{d}_{12}^{SVD} and the 265 ENM(S₂), revealing that the energy pathway is mainly dictated by this mode. **Figure 5(c)** shows the distribution of values of participation number PN^α (defined by eq. 14) obtained from the set of \mathbf{d}_{12} at the moment of effective S₂→S₁ transition for each NEXMD trajectories. While \mathbf{d}_{12} vectors are superimposed by several ENMs(S₁) ($PN^1 \approx 10 - 15$), they are highly localized on one single ENM(S₂), that is, the 265 ENMs(S₂) ($PN^2 \approx 1$). That is, the energy relaxation of LPPP5-PMI takes place through a unique relaxation pathway described by a single ENMs(S₂) that engages multiple ENMs(S₁).

At this point it is important to note that results analyzed in terms of the effective simulation time, as the ones shown in **Figures 4**, are not the most adequate to elucidate the vibrational energy transfer process. This is because the S₂→S₁ electronic energy transfer takes place at different times during NEXMD trajectories, hiding details related the concomitant mechanism of vibrational energy redistribution. In order to gain a better insight on the vibrational energy flux during the S₂→S₁ electronic energy transfer, we monitor $\langle E_i(t) \rangle$, as a function of delay time, $\tau = t - t_{\text{hop}}$, relative to the hopping time from S₂ to S₁ potential energy surface. Active normal modes can be identified by analyzing the maximum value of $\langle E_i(\tau) \rangle$ reached by each mode during our NEXMD simulations ($\langle E_i^{\text{max}}(\tau) \rangle$). In this way, each mode can be associated to its corresponded $\langle E_i^{\text{max}}(\tau) \rangle$ and, therefore, a distribution of the relative probability for these values is built and fitted to a Gaussian distribution. A normal mode is defined as active if its maximum value of $\langle E_i^{\text{max}}(\tau) \rangle$ is at $+2\sigma$ (being σ the standard distribution) of the distribution of $\langle E_i^{\text{max}}(\tau) \rangle$ values for all the modes. The corresponding distributions of $\langle E_i^{\text{max}}(\tau) \rangle$ for either ENMs(S₁) and ENMs(S₂) are shown in **Figure S3**. **Tables 1** and **2** present the list of ENMs(S₁) and ENMs(S₂) respectively that fulfill this criterium. They represent the modes with the most significant transient accumulation of vibrational energy. **Figure 6** shows $\langle E_i(\tau) \rangle$ for these selected active modes from this set. We can classify them as initial (I) (**Figure 6(a)**), earlier (E) (**Figure 6(b)**), and late (L) excited active modes (**Figure 6(c)**). The I modes correspond to those modes that are vibrationally excited at the moment of the S₂→S₁ electronic energy transfer. These modes transfer their energy to the E modes in a wave-like manner. Finally, L modes represent a set of active modes whose excess of energy larger than kT appears due to the vibrational energy redistribution on S₁ state PES, not due to ‘inheritance’ of energy from I modes.

Energy-wise, the active modes are middle to high-frequency vibrations, most of them lay within the [1500, 2000] cm⁻¹ region. They represent a set of modes with distinctly different spatial localization. **Tables 1** and **2** show the fraction of each i -th active normal mode on the donor, calculated as $\sum_{j \in \text{donor}}^{3N} (l_{ji}^\alpha)^2$. The high-frequency 265 ENM(S₂) ($\nu=2378$ cm⁻¹) is the I active mode with the strongest participation in the intramolecular energy transfer. This mode is delocalized between donor and acceptor moieties, having ~ 0.6 of localization in the donor. Its delocalization between both moieties guarantees the donor-acceptor vibronic coupling required for an effective energy transfer. 235 ENM(S₁) ($\nu=1622$ cm⁻¹) and 239 ENM(S₂) ($\nu=1685$ cm⁻¹) are the main E active modes. As expected for the E modes, they are mainly localized on the acceptor moiety, having only 0.11 and 0.24 of delocalization fraction to the donor, respectively.

It is interesting at this point to examine the correspondence between the sets of ENMs(S₂) and ENMs(S₁) by analyzing the **O** matrix after its rearrangement using the Min-Cost method (see Section II. B). **Figure 7** shows the **O** matrix. We notice that most of the modes have singular *one-to-one* correspondence in the two states. The exceptions are vibrations

previously identified as active modes. This is the case of 265, 239 and 235 ENMs(S_2) that are actually superimposed by several ENMs(S_1). These features explain the main differences in the transient accumulation of the excess of vibrational energy between active ENMs(S_1) and ENMs(S_2) shown in **Figures 4(a)** and **(c)**. In the particular case of the 265 ENM(S_2), it is expanded among ~ 20 ENMs(S_1) including all the active ENMs(S_1) listed in **Table 1**.

Let us now to quantify the two evaluated criteria that contribute to systematically identify and characterize the active modes: (i) the contribution of each normal mode to the direction of $NACR_{12}$ during electronic transitions, quantified by considering those normal modes that are within the first PN^α modes ordered in decreasing values of $\sqrt{\langle (\mathbf{Q}_i^\alpha \cdot \mathbf{d}_{12})^2 \rangle}$ in all trajectories; (ii) the transient accumulation of excess energy in individual normal modes, quantified by considering those normal modes whose values of $\langle E_i^{max}(\tau) \rangle$ are at $+2\sigma$ of the distribution of $\langle E_i^{max}(\tau) \rangle$ values for all the modes. **Tables 1** and **2** summarize these values for active modes defined according to both criteria. A significant overlap between both criteria, shown for ENMs(S_1), indicates that normal modes that contribute the most to the direction of $NACR_{12}$ commonly correspond to the ones that transiently accumulate the largest amount of excess of vibrational energy. Nevertheless, the identities of these modes significantly change according to the PES on which the ENMs are evaluated. Both criteria do not overlap and actually they complement each other for ENMs(S_2), where 265 ENM(S_2) is the unique I active mode. 235 and 239 ENMs(S_2) are E active modes that do not participate of the direction of energy transfer.

Once active normal modes have been identified, we can analyze their contribution to the non-adiabatic coupling terms ($NACT_{12}$) defined as $\dot{\mathbf{R}} \cdot \mathbf{d}_{12}$. $NACT_{12}$ values are ultimately responsible for the change of electronic populations on time (see eq. 3). In order to do that, $NACT_{\alpha\beta}$ can be expressed as

$$NACT_{\alpha\beta} = \sum_{i=1}^{3N-6} \dot{\mathbf{Q}}_i^\alpha \cdot \mathbf{d}_{\alpha\beta} \quad (17)$$

and eq. 13 is used in order to express $\mathbf{d}_{\alpha\beta}$ onto the ENM(S_α), being $\alpha, \beta=1,2$. **Tables 1** and **2** show the average of the absolute values of the different contributions $\langle |\dot{\mathbf{Q}}_i^\alpha \cdot \mathbf{d}_{12}| \rangle$ for the set of selected active modes. In all cases, active ENMs(S_1) are within the ones that contribute the most to $NACT_{12}$ during electronic transitions, indicating that active normal modes are within the main nuclear motions that couple both states. Besides, this analysis confirms that 235 and 239 ENMs(S_2), previously identified as E modes, do not contribute to the coupling between states.

Finally, it is important to point out that active normal modes are modes that experience the largest energy exchange during $S_2 \rightarrow S_1$ transitions. This can be quantified by the values of their average change of kinetic energy during $S_2 \rightarrow S_1$ effective hops ($\langle \Delta E_i^{S_2 \rightarrow S_1} \rangle$), expressed in % of the total kinetic energy redistributed over all modes (see **Tables 1** and **2**). As it is expected, while the energy is spread among the several active ENMs(S_1), the energy transfer is funneled mainly through the 265 ENM(S_2).

In order to further explore the vibrational energy redistribution during donor-acceptor electronic energy transfer, the SMF method⁸⁶, previously described in Section IID, has been applied. **Figure 8** shows the accumulated flux for active modes arranged as bundles of I, E, and L active modes, previously classified in **Figure 6**. The SMF method has been applied using either ENMs(S_1) and ENM(S_2). In both cases, two different vibrational energy redistribution

pathways can be observed: (a) a direct I→L transfer pathway, in which the I active modes transfer their excess of vibrational energy directly to the L active modes, and (b) a sequential I→E→L transfer pathway in which the energy flow through the intermediate E active modes. **Figure 8** shows that the sequential pathway represents the main mechanism of intramolecular vibrational energy redistribution during donor-acceptor electronic energy transfer, being the direct I→L transfer almost negligible when ENM(S_2) are considered.

A qualitative picture of the donor→acceptor vibronic energy transfer that takes place during the S_2 → S_1 internal conversion can be described as following: The process takes place through a unique pathway, involving a common principal direction of energy flux in the S_2 PES. This direction is defined by the 265 ENM(S_2), which is the main vibrational mode coupled to the donor→acceptor energy transfer. After S_2 → S_1 transition, the excess of vibrational energy becomes distributed across multiple vibrational motions on the S_1 PES, that ultimately relax to the rest of the nuclei degrees of freedom of the molecule.

IV. CONCLUSIONS

Non-adiabatic excited state molecular dynamics calculations have been performed on a model donor-acceptor system to decipher the role of vibrational energy redistribution during the S_2 → S_1 internal conversion process. While the S_2 state is mainly localized on the donor moiety, the S_1 is localized on the acceptor unit. Therefore, an ultrafast S_2 → S_1 (i.e. donor→acceptor), both electronic and vibrational energy transfer takes place immediately after photoexcitation.

Our analysis of vibrational energies associated with individual normal modes, calculated on the S_1 and S_2 PES, indicates that only a few normal modes, the so-called active modes, transiently accumulate an excess of vibrational energy. These active modes are distinguished by the most significant rearrangements and mixing according to the PES on which they are obtained. The remaining molecular vibrations seem to act as a bath of coupled harmonic oscillators, which ultimately absorbs the excess energy.

The intramolecular vibrational energy transfer takes place through two distinguished pathways: direct and sequential, involving a common principal direction of energy flux in the S_2 PES. This direction is given by a singular high-frequency ENM(S_2), which immediately accepts a significant electronic energy and is responsible for the donor→acceptor vibrational energy transfer. This mode is completely delocalized between the donor and acceptor moieties and its direction is roughly aligned with the non-adiabatic coupling vector. Once the excess of vibrational energy is transferred to the S_1 PES, it becomes scattered among several ENMs(S_1) mainly localized on the acceptor segment. These modes finally relax by distributing their energy to later excited modes and ultimately to the rest of the molecular vibrations.

Two criteria contribute to systematically identify and characterize the subset of vibrational normal modes that actively participate on the electronic relaxation: the overlap of individual normal modes with the direction of $NACR_{\alpha\beta}$ during electronic transitions and their transient accumulation of excess energy during the subsequent intramolecular vibrational energy redistribution. Both criteria provide complementary information. Future analysis of other molecular systems featuring energy transfer channels will elucidate to which extent our findings relate to changes in the efficiency of donor→acceptor energy transfer. Nevertheless, these results clearly single out the importance of a specific vibrational motion of the donor and

the corresponding excited state normal mode in principle could be treated quantum-mechanically. We recognize that this may improve energy transfer simulations by including quantum effects such as tunneling and vibrational quantum transfer.

Acknowledgements

This work was partially supported by CONICET, UNQ, ANPCyT (PICT-2018-2360), the Universidad Carlos III de Madrid, the European Union's Seventh Framework Programme for research, technological development and demonstration under grant agreement No. 600371, el Ministerio de Economía, Industria y Competitividad (COFUND2014-51509), el Ministerio de Educación, cultura y Deporte (CEI-15-17), Banco Santander and el Ministerio de Ciencia, Innovación y Universidades (RTI2018-101020-B-I00). We also acknowledge support from the Bavarian University Centre for Latin America (BAYLAT). The work at Los Alamos National Laboratory (LANL) was supported by the Laboratory Directed Research and Development Funds (LDRD) program. This work was done in part at the Center for Nonlinear Studies (CNLS) and the Center for Integrated Nanotechnologies (CINT), a U.S. Department of Energy and Office of Basic Energy Sciences user facility, at LANL. This research used resources provided by the LANL Institutional Computing Program. Los Alamos National Laboratory is operated by Triad National Security, LLC, for the National Nuclear Security Administration of the U.S. Department of Energy. This work has received financial support provided by the Spanish Agencia Estatal de Investigación (AEI) and Fondo Europeo de Desarrollo Regional (FEDER, UE) under Project CTQ2016-79345-P and by the Fundación Séneca under Project 20789/PI/18.

Table 1. Active ENMs(S_1) defined as (i) those normal modes whose values of $\langle E_i^{max}(\tau) \rangle$ are at $+2\sigma$ of the distribution of $\langle E_i^{max}(\tau) \rangle$ values for all the modes and as (ii) those normal modes that are within the first PN^1 modes ordered in decreasing values of $\sqrt{\langle (\mathbf{Q}_i^1 \cdot \mathbf{d}_{12})^2 \rangle}$ in all trajectories. Only modes that fulfill any of these criteria are listed. $\langle \Delta E_i^{S_2 \rightarrow S_1} \rangle$ represents the average change of kinetic energy for the i th mode during $S_2 \rightarrow S_1$ effective hops, expressed in % of the total kinetic energy redistributed over all modes. $\sqrt{\langle (\mathbf{Q}_i^1 \cdot \mathbf{d}_{12})^2 \rangle}$ is the root mean square, calculated over all the trajectories, of the overlap (inner product) between \mathbf{Q}_i^1 and of \mathbf{d}_{12} evaluated at the moment of effective $S_2 \rightarrow S_1$ transitions (hops). $\langle |\dot{\mathbf{Q}}_i^1 \cdot \mathbf{d}_{12}| \rangle$ is the average of the absolute value of the contribution of each i th active modes to \mathbf{d}_{12} .

mode # (ν [cm^{-1}])	$\langle E_i^{max}(\tau) \rangle$ [eV]	Fraction of localization in donor	$\langle \Delta E_i^{S_2 \rightarrow S_1} \rangle$ %	$\sqrt{\langle (\mathbf{Q}_i^1 \cdot \mathbf{d}_{12})^2 \rangle}$	$\langle \dot{\mathbf{Q}}_i^1 \cdot \mathbf{d}_{12} \rangle$
227 (1579)	0.073	0.93	7.2	0.31	0.30
231 (1597)	0.057	0.39	4.2	0.24	0.18
235 (1622)	0.088	0.11	4.2	0.25	0.20
250 (1773.8)	0.052	0.56	7.6	0.29	0.23
251 (1774.5)	0.046	0.42	13.9	0.27	0.19
252 (1776.4)	0.048	0.00	2.3	0.24	0.17
258 (1818)	0.087	1.00	22.2	0.45	0.40

Table 2. Same as Table 1 but for active ENMs(S_2).

mode # (ν [cm^{-1}])	$\langle E_i^{max}(\tau) \rangle$ [eV]	Fraction of localization in donor	$\langle \Delta E_i^{S_2 \rightarrow S_1} \rangle$ %	$\sqrt{\langle (\mathbf{Q}_i^2 \cdot \mathbf{d}_{12})^2 \rangle}$	$\langle \dot{\mathbf{Q}}_i^2 \cdot \mathbf{d}_{12} \rangle$
235 (1646)	0.048	0.11	0.0	0.01	0.01
239 (1685)	0.094	0.24	0.0	0.02	0.01
265 (2378)	0.287	0.59	85.9	0.93	0.89

Bibliography

- 1 P. Wilhelm, J. Schedlbauer, F. Hinderer, D. Hennen, S. Höger, J. Vogelsang and J. Lupton, Molecular excitonic seesaws, *Proc Natl Acad Sci USA*, 2018, **115**, E3626–E3634.
- 2 O. Mikhnenko, P. Blom and T. Nguyen, Exciton diffusion in organic semiconductors., *Energy Environ. Sci.*, 2015, **8**, 1867–1888.
- 3 T. Brixner, R. Hildner, J. Köhler, C. Lambert and F. Würthner, Exciton Transport in Molecular Aggregates – From Natural Antennas to Synthetic Chromophore Systems, *Adv. Energy Mater.*, 2017, **7**, 1700236–1700269.
- 4 M. Ansari-Rad and S. Athanasopoulos, Theoretical study of equilibrium and nonequilibrium exciton dynamics in disordered semiconductors., *Phys. Rev. B*, 2018, **98**, 085204.
- 5 C. Bardeen, The Structure and Dynamics of Molecular Excitons, *Ann. Rev. Phys. Chem.*, 2014, **65**, 127–148.
- 6 A. Aggarwal, A. Thiessen, A. Idelson, D. Kalle, D. Würsch, T. Stangl, F. Steiner, S.-S. Jester, J. Vogelsang, S. Höger and J. Lupton, Fluctuating exciton localization in giant π -conjugated spoked-wheel macrocycles, *Nat Chem.*, 2013, **5**, 964–970.
- 7 G. Scholes, G. Fleming, A. Olaya-Castro and R. van Grondelle, Lessons from nature about solar light harvesting, *Nat. Chem.*, 2011, **3**, 763–774.
- 8 A. Köhler and H. Bässler, *Electronic Processes in Organic Semiconductors: An Introduction*, John Wiley & Sons, Weinheim, Germany, 2015.
- 9 O. Inganäs, Organic Photovoltaics over Three Decades., *Adv. Mater.*, 2018, **30**, 1800388.
- 10 B. Lasorne, F. Sicilia, M. J. Bearpark, M. a Robb, G. a Worth and L. Blancafort, Automatic generation of active coordinates for quantum dynamics calculations: application to the dynamics of benzene photochemistry., *J. Chem. Phys.*, 2008, **128**, 124307.
- 11 M. a Soler, A. E. Roitberg, T. Nelson, S. Tretiak and S. Fernandez-Alberti, Analysis of state-specific vibrations coupled to the unidirectional energy transfer in conjugated dendrimers., *J. Phys. Chem. A*, 2012, **116**, 9802–10.
- 12 J. F. Galindo, S. Fernandez-Alberti and A. E. Roitberg, Electronic excited state specific IR spectra for phenylene ethynylene dendrimer building blocks, *J. Phys. Chem. C*, 2013, **117**, 26517–26528.
- 13 M. . Saab, L. J. . Doriol, B. . Lasorne, S. . Guerin and F. Gatti, A quantum dynamics study of the benzopyran ring opening guided by laser pulses., *Chem. Phys.*, 2014, **442**, 93–102.
- 14 B. Lasorne, G. a. Worth and M. a. Robb, Excited-state dynamics, *Wiley Interdiscip. Rev. Comput. Mol. Sci.*, 2011, **1**, 460–475.
- 15 Y. . Chen, P. M. . Palmer and M. R. Topp, Infrared Spectroscopy of Jetcooled, Electronically Excited Clusters of Coumarin 151: Excited state Interactions and Conformational Relaxation., *Int. J. Mass Spectrom.*, 2002, **220**, 231–251.
- 16 M. . Weiler, K. . Bartl and M. Gerhards, Infrared/ultraviolet Quadruple Resonance Spectroscopy to Investigate Structures of Electronically Excited States., *J. Chem. Phys.*, 2012, **136**, 114202.
- 17 N. . Seurre, K. . Le Barbu-Debus, F. . Lahmani, A. . Zehnacker-Rentien and J. Sepiol, Electronic and Vibrational Spectroscopy of Jetcooled Mcyanophenol and Its Dimer: Laser-induced Fluorescence and Fluorescence-dip IR Spectra in the S0 and S1 States.,

- Chem. Phys.*, 2003, **295**, 21–33.
- 18 J. Hill, C. Ziegler, K. Suslick, D. Dlott, C. Rella and M. Fayer, Tuning the vibrational relaxation of co bound to heme and metalloporphyrin complexes., *J Phys Chem*, 1996, **100**, 18023–18032.
- 19 P. Hamm, M. Lim and R. M. Hochstrasser, Structure of the Amide I Band of Peptides Measured by Femtosecond Nonlinear-Infrared Spectroscopy, 1998, **5647**, 6123–6138.
- 20 K. a. Peterson, C. W. Rella, J. R. Engholm and H. a. Schwettman, Ultrafast Vibrational Dynamics of the Myoglobin Amide I Band, *J. Phys. Chem. B*, 1999, **103**, 557–561.
- 21 D. D. Dlott, Vibrational energy redistribution in polyatomic liquids: 3D infrared–Raman spectroscopy, *Chem. Phys.*, 2001, **266**, 149–166.
- 22 L. Iwaki and D. Dlott, in *Encyclopedia of chemical physics and physical chemistry.*, eds. J. Moore and N. Spencer, Bristol, P Publishi., 2001, p. 2717.
- 23 M. Fayer, Fast protein dynamics probed with infrared vibrational echo experiments., *Annu Rev Phys Chem*, 2001, **52**, 315.
- 24 M. Fayer, *Ultrafast infrared and Raman spectroscopy.*, Marcel Dekker Inc, New York, 2001.
- 25 M. Cremeens, H. Fujisaki, Y. Zhang, J. Zimmermann, L. Sagle, S. Matsuda, P. Dawson, J. Straub and F. Romesberg, Efforts toward developing direct probes of protein dynamics., *J Am Chem Soc*, 2006, **128**, 6028–6029.
- 26 S. Shigeto and D. D. Dlott, Vibrational relaxation of an amino acid in aqueous solution, *Chem. Phys. Lett.*, 2007, **447**, 134–139.
- 27 Z. Wang, J. Carter, A. Lagutchev, Y. Koh, N.-H. Seong, D. Cahill and D. Dlott, Ultrafast flash thermal conductance of molecular chains., *Science (80-.)*, 2007, **317**, 787.
- 28 S. Shigeto, Y. Pang, Y. Fang and D. D. Dlott, Vibrational relaxation of normal and deuterated liquid nitromethane., *J. Phys. Chem. B*, 2008, **112**, 232–41.
- 29 M. Schade, A. Moretto, M. Crisma, C. Toniolo and P. Hamm, Vibrational energy transport in peptide helices after excitation of c-d modes in leu-d10., *J Phys Chem A*, 2009, **113**, 13393–13397.
- 30 Y. Fang, S. Shigeto, N. Seong and D. D. Dlott, Vibrational Energy Dynamics of Glycine, N-Methylacetamide, and Benzoate Anion in Aqueous (D₂O) Solution Vibrational Energy Dynamics of Glycine, N-Methylacetamide, and Benzoate Anion in Aqueous (D₂O) Solution.
- 31 Y. Zhang, J. Kubicki and P. MS, Ultrafast UV-Visible and Infrared Spectroscopic Observation of a Singlet Vinylcarbene and the Intramolecular Cyclopropanation Reaction., *J. Am. Chem. Soc.*, 2009, **131**, 13602–13603.
- 32 Y. Zhang, G. Burdzinski, J. Kubicki, S. Vyas, C. M. Hadad, M. Sliwa, O. Poizat, G. Buntinx and M. S. Platz, Study of the S1 Excited State of para-Methoxy-3-phenyl-3-methyl Diazirine by Ultrafast Time Resolved UV-Vis and IR Spectroscopies and Theory., *J. Am. Chem. Soc.*, 2009, **131**, 13784–13790.
- 33 S. Vyas, J. Kubicki, H. L. Luk, Y. Zhang, N. P. Gritsan, C. M. Hadad and M. S. Platz, An Ultrafast Time-resolved Infrared and UV-vis Spectroscopic and Computational Study of the Photochemistry of Acyl Azides., *J. Phys. Org. Chem.*, 2012, **25**, 693–703.
- 34 T. P. Dougherty and E. J. Heilweil, Ultrafast Transient Infrared Absorption Studies of M(CO)₆ (M = Cr, Mo or W) Photoproducts in N-hexane Solution., *Chem. Phys. Lett.*, 1994, **227**, 19–25.
- 35 P. H. Nguyen and G. Stock, Nonequilibrium molecular-dynamics study of the vibrational energy relaxation of peptides in water, 2003, **119**, 11350–11358.

- 36 C. Brooks III, M. Karplus and B. M. Pettitt, *Proteins: A theoretical perspective of dynamics, structure, and thermodynamics*, John Wiley & Sons Ltd, Advances i., 1987.
- 37 T. Nishikawa and N. Gō, Normal modes of vibration in bovine pancreatic trypsin inhibitor and its mechanical property., *Proteins Struct., Funct., Genet.*, 1987, **2**, 308–329.
- 38 B. Brooks and M. Karplus, Harmonic dynamics of proteins: normal modes and fluctuations in bovine pancreatic trypsin inhibitor., *Proc. Natl. Acad. Sci. U. S. A.*, 1983, **80**, 6571–6575.
- 39 J. Andrew McCammon and S. C. Harvey, *Dynamics of proteins and nucleic acids.*, Cambridge University Press, 1987.
- 40 L. Kurtz, A. Hofmann and R. De Vivie-riedle, Ground state normal mode analysis : Linking excited state dynamics and experimental observables, *J. Chem. Phys.*, 2001, **114**, 6151–6159.
- 41 G. a Worth and L. S. Cederbaum, Beyond Born-Oppenheimer: molecular dynamics through a conical intersection., *Annu. Rev. Phys. Chem.*, 2004, **55**, 127–58.
- 42 S. Fernandez-Alberti, A. E. Roitberg, T. Nelson and S. Tretiak, Identification of unavoided crossings in nonadiabatic photoexcited dynamics involving multiple electronic states in polyatomic conjugated molecules., *J. Chem. Phys.*, 2012, **137**, 014512.
- 43 M. Z. Zgierski, On mode mixing effects in absorption-emission spectra and resonance raman excitation profiles, *Chem. Phys.*, 1986, **108**, 61–68.
- 44 J. J. Newby, C. Liu, P. Rodrigo, C. W. Mu and T. S. Zwier, Duschinsky mixing between four non-totally symmetric normal coordinates in the S 1 – S 0 vibronic structure of (E) -phenylvinylacetylene : a quantitative analysis, *Phys. Chem. Cehmical Phys.*, 2010, **12**, 2331–2343.
- 45 G. Orr and G. Small, Vibronic intensity borrowing and the isotope dependence of vibronic structure, *Chem. Phys.*, 1973, 60.
- 46 F. Metz, M. J. Robey, E. W. Schlag and F. Dorr, Vibronic coupling and the Duschinsky effect in benzene, 1977, **51**, 8–12.
- 47 W. Siebrand and M. Zgierski, The dushinsky effect in resonance Raman spectroscopy, *Chem. Phys. Lett.*, 1979, **62**, 3–8.
- 48 Franck–Condon effects in resonance Raman spectra and excitation profiles, *J. Chem. Phys.*, 1979, **71**, 3561.
- 49 J. Tonks, DL; Page, General theory of vibrational mode mixing and frequency shifts in resonance raman scattering, *Chem. Phys. Lett.*, 1981, **79**, 247.
- 50 C. Chan, J. Page, D. Tonks, O. Brafman, B. Khodadoost and C. Walker, Resonance Raman scattering study of azulene. II. Nonzero temperature multimode model calculations, *J. Chem. Phys.*, 1985, **82**, 4813.
- 51 D. W. Noid, M. L. Koszykowski and R. A. Marcus, Quasiperiodic and Stochastic Behavior in Molecules., *Annu. Rev. Phys. Chem.*, 1981, **32**, 267–309.
- 52 I. P. A. Schulz, S. Sudbo, D. J. Krajnovich, H. S. Kwok, Y. R. Shen and Y. T. Lee, Multiphoton dissociation of polyatomic molecules., *Annu. Rev. Phys. Chem.*, 1979, **30**, 379–409.
- 53 J. D. McDonald, Creation and disposal of vibrational energy in polyatomic molecules., *Annu. Rev. Phys. Chem.*, 1979, **30**, 29–50.
- 54 J. Singh and E. R. Bittner, Isotopic effect and temperature dependent intramolecular excitation energy transfer in a model donor – acceptor dyad, *Phys. Chem. Chem. Phys.*, 2010, **12**, 7418–7426.
- 55 X. Yang, T. Keane, M. Delor, A. J. H. M. Meijer, J. Weinstein and E. R. Bittner,

- Identifying electron transfer coordinates in donor-bridge-acceptor systems using mode projection analysis, *Nat. Comm.*, 2017, **8**, 1–8.
- 56 E. R. Bittner, An effective Hamiltonian approach for Donor-Bridge-Acceptor electronic transitions: Exploring the role of bath memory, *Condens. Matter Phys.*, 2016, **19**, 1–9.
- 57 X. Yang and E. R. Bittner, Intramolecular Charge- and Energy-Transfer Rates with Reduced Modes: Comparison to Marcus Theory for Donor – Bridge – Acceptor Systems, *J. Phys. Chem. A*, 2014, **118**, 5196–5203.
- 58 X. Yang, E. R. Bittner, X. Yang and E. R. Bittner, Computing intramolecular charge and energy transfer rates using optimal modes, *J. Chem Phys.*, 2015, **142**, 244114.
- 59 S. Athanasopoulos, L. Alfonso Hernandez, D. Beljonne, S. Fernandez-Alberti and S. Tretiak, Ultrafast Non-Förster Intramolecular Donor-Acceptor Excitation Energy Transfer, *J. Phys. Chem. Lett.*, DOI:10.1021/acs.jpcclett.7b00259.
- 60 T. Nelson, S. Fernandez-alberti, V. Chernyak, A. E. Roitberg and S. Tretiak, Nonadiabatic Excited-State Molecular Dynamics Modeling of Photoinduced Dynamics in Conjugated Molecules, *J. Phys. Chem. B*, 2011, **115**, 5402–5414.
- 61 T. Nelson, S. Fernandez-Alberti, A. E. Roitberg and S. Tretiak, Nonadiabatic Excited State Molecular Dynamics: Modeling Photophysics in Organic Conjugated Materials, *Acc. Chem. Res.*, 2014, **47**, 1155–1164.
- 62 J. C. Tully, Molecular dynamics with electronic transitions, *J. Chem Phys.*, 1990, **93**, 1061–1071.
- 63 S. Hammes-schiffer and J. C. Tully, Proton transfer in solution : Molecular dynamics with quantum transitions, *J. Chem Phys.*, 1994, **101**, 4657–4667.
- 64 T. Nelson, S. Fernandez-alberti, A. E. Roitberg and S. Tretiak, Nonadiabatic Excited-State Molecular Dynamics : Treatment of Electronic Decoherence, *J. Chem. Phys.*, 2013, **138**, 224111.
- 65 S. Tretiak and S. Mukamel, Density matrix analysis and simulation of electronic excitations in conjugated and aggregated molecules, *Chem. Rev.*, 2002, **102**, 3171–3212.
- 66 V. Chernyak, M. F. Schulz, S. Mukamel, S. Tretiak and E. V Tsiper, Krylov-space algorithms for time-dependent Hartree-Fock and density functional computations, *J. Chem. Phys.*, 2000, **113**, 36.
- 67 S. Tretiak, C. M. Isborn, A. M. N. Niklasson and M. Challacombe, Representation independent algorithms for molecular response calculations in time-dependent self-consistent field theories, *J. Chem. Phys.*, 2009, **130**, 054111–054127.
- 68 F. Furche and R. Ahlrichs, Adiabatic time-dependent density functional methods for excited state properties, *J. Chem. Phys.*, 2002, **117**, 7433–7448.
- 69 S. Tretiak and V. Chernyak, Resonant nonlinear polarizabilities in the time-dependent density functional theory, *J. Chem. Phys.*, 2003, **119**, 8809–8823.
- 70 M. Tommasini, V. Chernyak and S. Mukamel, Electronic density-matrix algorithm for nonadiabatic couplings in molecular dynamics simulations, *Int. J. Quantum Chem.*, 2001, **85**, 225–238.
- 71 V. Chernyak and S. Mukamel, Density-matrix representation of nonadiabatic couplings in time-dependent density functional (TDDFT) theories, *J. Chem. Phys.*, 2000, **8**, 3572–3579.
- 72 R. Send and F. Furche, First-order nonadiabatic couplings from time-dependent hybrid density functional response theory: Consistent formalism, implementation, and performance, *J. Chem. Phys.*, 2010, **132**, 044107–044119.
- 73 S. Mukamel, S. Tretiak, T. Wagersreiter and V. Chernyak, Electronic coherence and

- collective optical excitations of conjugated molecules, *Science* (80-.), 1997, **277**, 781–787.
- 74 S. Tretiak, V. Chernyak and S. Mukamel, Recursive density-matrix-spectral-moment algorithm for molecular nonlinear polarizabilities, *J. Chem. Phys.*, 1996, **105**, 8914–8928.
- 75 S. Tretiak, W. M. Zhang, V. Chernyak and S. Mukamel, Excitonic couplings and electronic coherence in bridged naphthalene dimers, *Proc. Nat. Acad. Sci. USA*, 1999, **96**, 13003–13008.
- 76 M. J. S. Dewar, E. G. Zoebisch, E. F. Healy and J. J. P. Stewart, The development and use of quantum-mechanical molecular-models.76.AM1 - A new general purpose quantum-mechanical molecular-model, *J. Am. Chem. Soc.*, 1985, **107**, 3902–3909.
- 77 S. Tretiak, V. Chernyak and S. Mukamel, Two-dimensional real-space analysis of optical excitations in acceptor-substituted carotenoids, *J. Am. Chem. Soc.*, 1997, **119**, 11408–11419.
- 78 S. Tretiak, V. Chernyak and S. Mukamel, Collective electronic oscillators for nonlinear optical response of conjugated molecules, *Chem. Phys. Lett.*, 1996, **259**, 55–61.
- 79 C. Wu, S. V Malinin, S. Tretiak and V. Y. Chernyak, Exciton scattering and localization in branched dendrimeric structures, *Nat. Phys.*, 2006, **2**, 631–635.
- 80 T. Nelson, S. Fernandez-Alberti, V. Chernyak, A. E. Roitberg and S. Tretiak, Nonadiabatic excited-state molecular dynamics: numerical tests of convergence and parameters., *J. Chem. Phys.*, 2012, **136**, 054108.
- 81 M. Soler, T. Nelson, A. Roitberg, S. Tretiak and S. Fernandez-Alberti, Signature of Nonadiabatic Coupling in Excited-State Vibrational Modes., *J. Phys. Chem. A*, 2014, **118**, 10372–10379.
- 82 A. Kalstein, S. Fernández-Alberti, A. Bastida, M. A. Soler, M. H. Farag, J. Zúñiga and A. Requena, Vibrational dynamics of polyatomic molecules in solution: assignment, time evolution and mixing of instantaneous normal modes, *Theor. Chem. Acc.*, 2010, **128**, 769–782.
- 83 G. Carpaneto, S. Martello and P. Toth, Algorithms and codes for the assignment problem, *Ann. Oper. Res.*
- 84 R. J. Bell, P. Dean and D. C. Hibbins-Butler, Localization of normal modes in vitreous silica, germania and beryllium fluoride, *J. Phys. C Solid St. Phys*, 1970, **3**, 2111–2118.
- 85 S. N. Taraskin and S. R. Elliott, Anharmonicity and localization of atomic vibrations in vitreous silica, *Phys. Rev. B*, 1999, **59**, 8572–8585.
- 86 M. A. Soler, A. Bastida, M. H. Farag, J. Zúñiga and A. Requena, A method for analyzing the vibrational energy flow in biomolecules in solution., *J. Chem. Phys.*, 2011, **135**, 204106.
- 87 S. Fernandez-Alberti, A. E. Roitberg, T. Nelson and S. Tretiak, Identification of unavoided crossings in nonadiabatic photoexcited dynamics involving multiple electronic states in polyatomic conjugated molecules., *J. Chem. Phys.*, 2012, **137**, 014512.
- 88 T. Nelson, S. Fernandez-alberti, V. Chernyak, A. E. Roitberg and S. Tretiak, Nonadiabatic Excited-State Molecular Dynamics Modeling of Photoinduced Dynamics in Conjugated Molecules.
- 89 T. Nelson, S. Fernandez-alberti, A. E. Roitberg and S. Tretiak, Nonadiabatic Excited-State Molecular Dynamics (NA-ESMD). Numerical tests of convergence and parameters.
- 90 T. Nelson, S. Fernandez-Alberti, A. E. Roitberg and S. Tretiak, Nonadiabatic excited-

state molecular dynamics: Modeling photophysics in organic conjugated materials, *Acc. Chem. Res.*, , DOI:10.1021/ar400263p.

Figure Captions

Figure 1. (a) Chemical structure of the LPPP5(donor)-PMI(acceptor) dyad system. The dihedral angle Φ that connects both moieties is defined; (b) Calculated equilibrated absorption spectrum of the LPPP5-PMI dyad at 300K showing contributions from the two lowest excited states; (c) Initial localization of the electronic transition densities for the two lowest excited states. Spatial distribution of electronic transition densities for S_1 and S_2 states calculated at the ground-state energy minimum.

Figure 2. (a) Time evolution of the average populations of electronic excited states during NEXMD simulations; (b) time evolution of the fraction of electronic transition density localized on the LPP5 donor and the PMI acceptor. Short time dynamics are shown as insets.

Figure 3. Histogram of the dihedral angle Φ values (a) at the beginning ($t=0$ fs), and (b) at the end ($t=1$ ps) of NEXMD simulations. Dashed lines represent Gaussian fitting centered at (a) 66° and 111° and (b) 51° and 130° . (c) time evolution of the contour density plot of Φ during the NEXMD simulations.

Figure 4. Evolution in time of the average over all NEXMD trajectories of vibrational energy, $\langle E_i(t) \rangle$, associated to (a) active ENMs(S_1) and (b) the rest of ENMs(S_1). (c) and (d) show the same as panels (a) and (b) but for ENMs(S_2).

Figure 5. (a) Direction of \mathbf{d}_{12}^{SVD} ; (b) distribution of the overlap between \mathbf{d}_{12}^{SVD} and the originals \mathbf{d}_{12} corresponding to each NEXMD trajectory; (c) distribution of values of PN^α obtained from the set of \mathbf{d}_{12} at the moment of effective $S_2 \rightarrow S_1$ transition in each NEXMD trajectories.

Figure 6. Average vibrational energy E_i during the NEXMD simulations as a function of delay time, $\tau = t - t_{\text{hop}}$, relative to the moment of non-adiabatic $S_2 \rightarrow S_1$ transition for (a) donor, (b) acceptor, and (c) late excited active modes. Dashed lines correspond to ENMs(S_2) and solid lines to ENMs(S_1).

Figure 7. Contour plot of the overlap matrix \mathbf{O} connecting the ENMs(S_2) and ENMs(S_1). The sizes of the bubbles are proportional to the values of $O_{ii'}$ elements. The different ENM(S_1) contributions to the main active ENM(S_2) are indicated in red for 265 ENM(S_2) and blue for 235 and 239 ENM(S_2).

Figure 8. Accumulated flux for donor (D), acceptor (A) and late excited (LE) active modes computed using the SMF method.

Figure 1

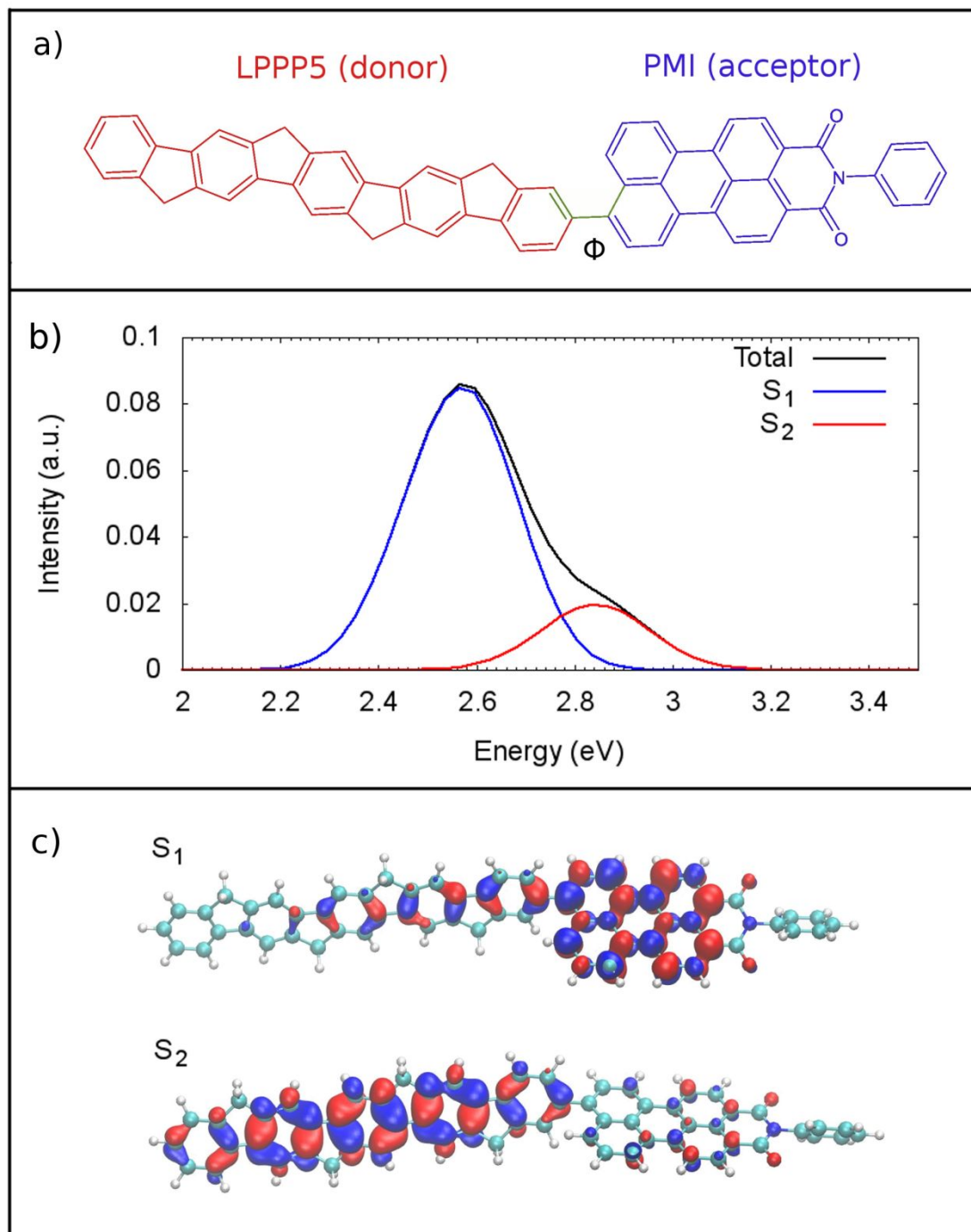


Figure 2

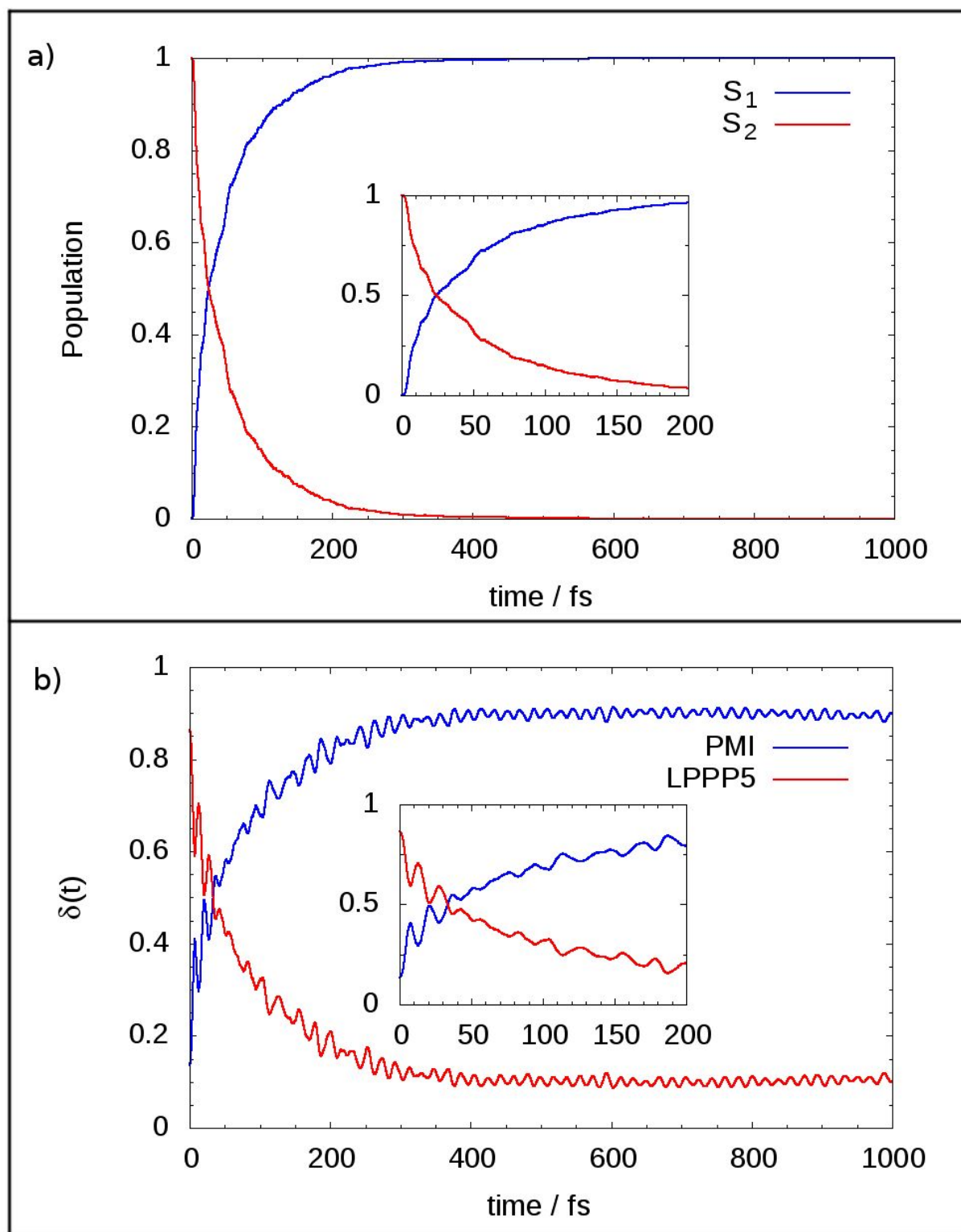


Figure 3

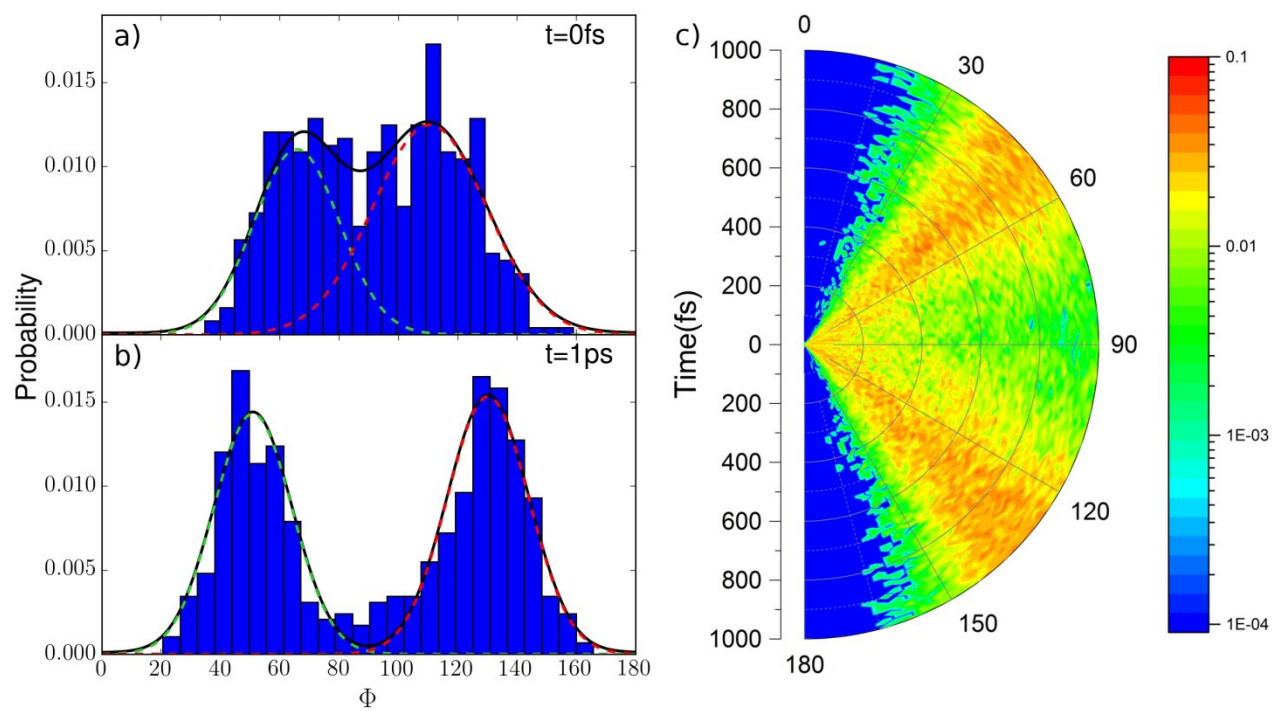


Figure 4

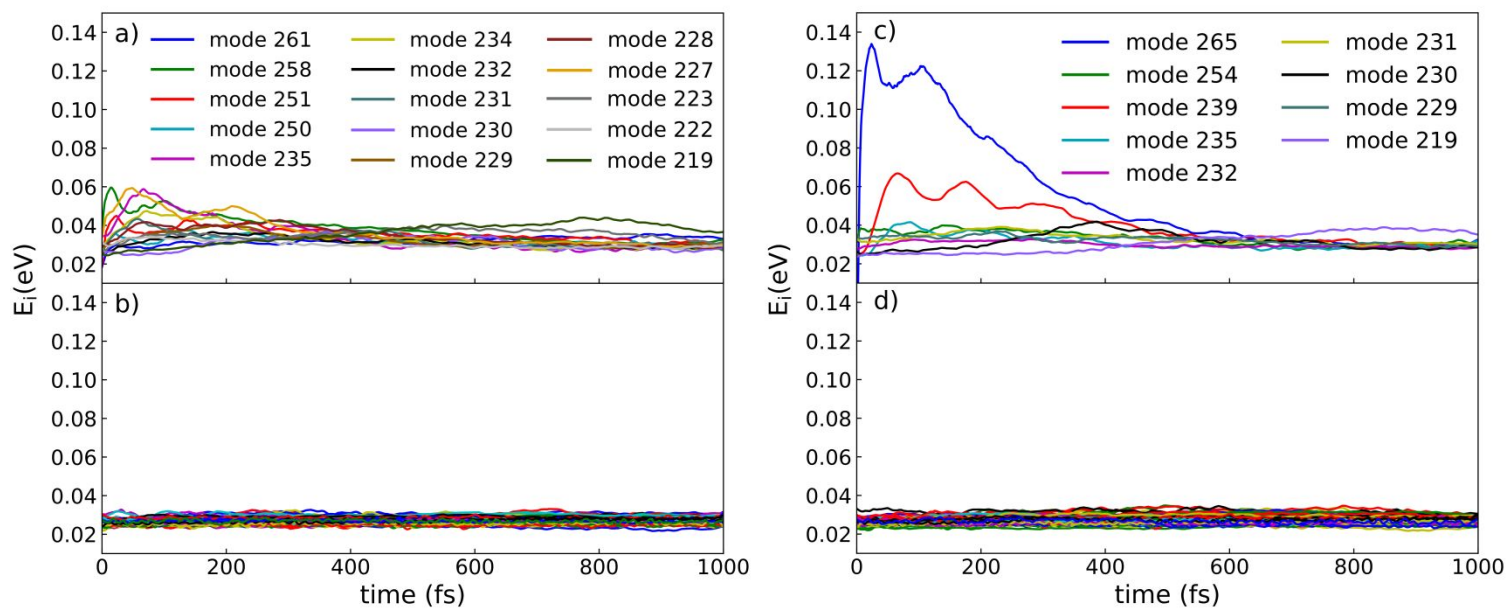


Figure 5

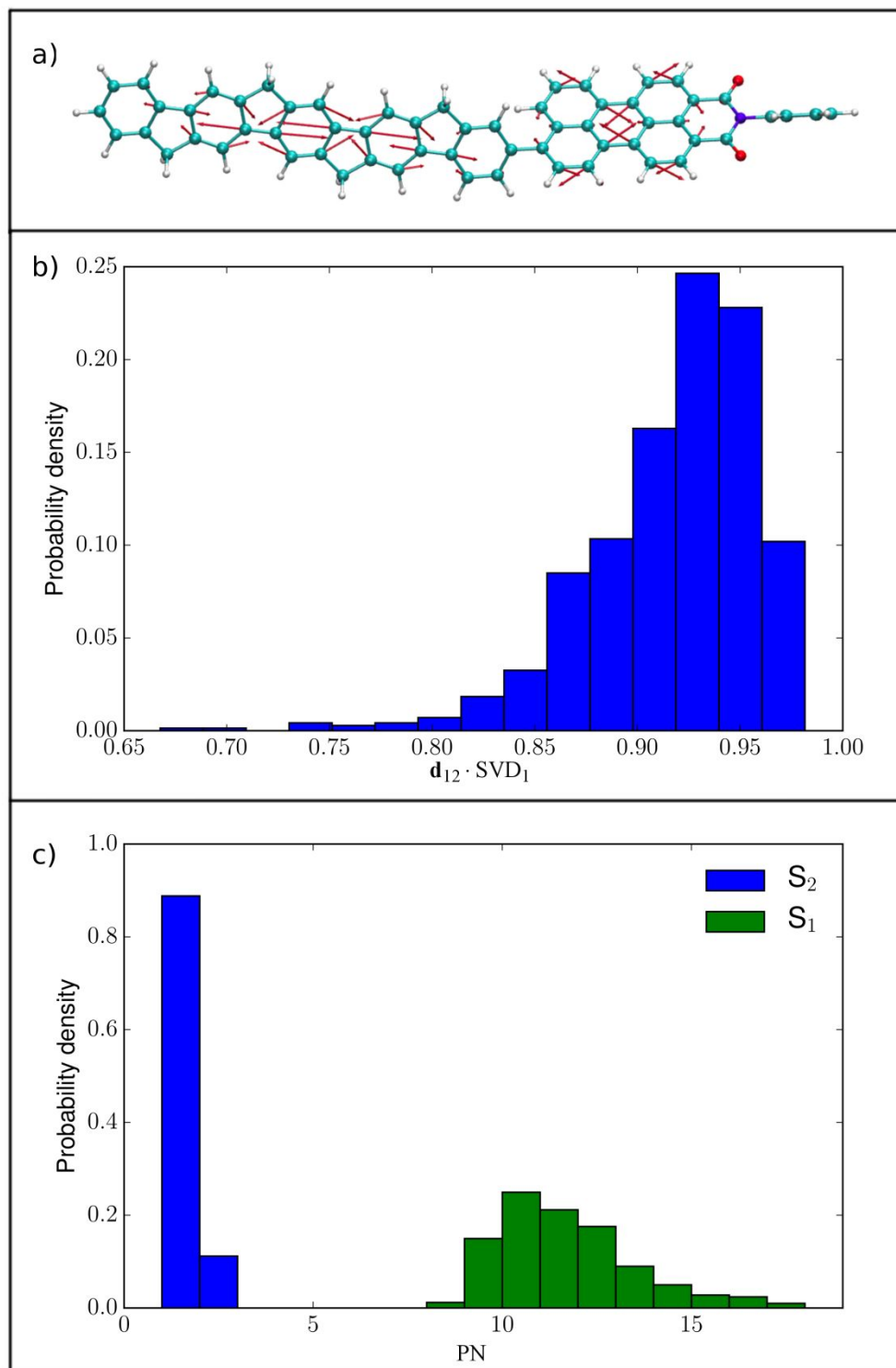


Figure 6

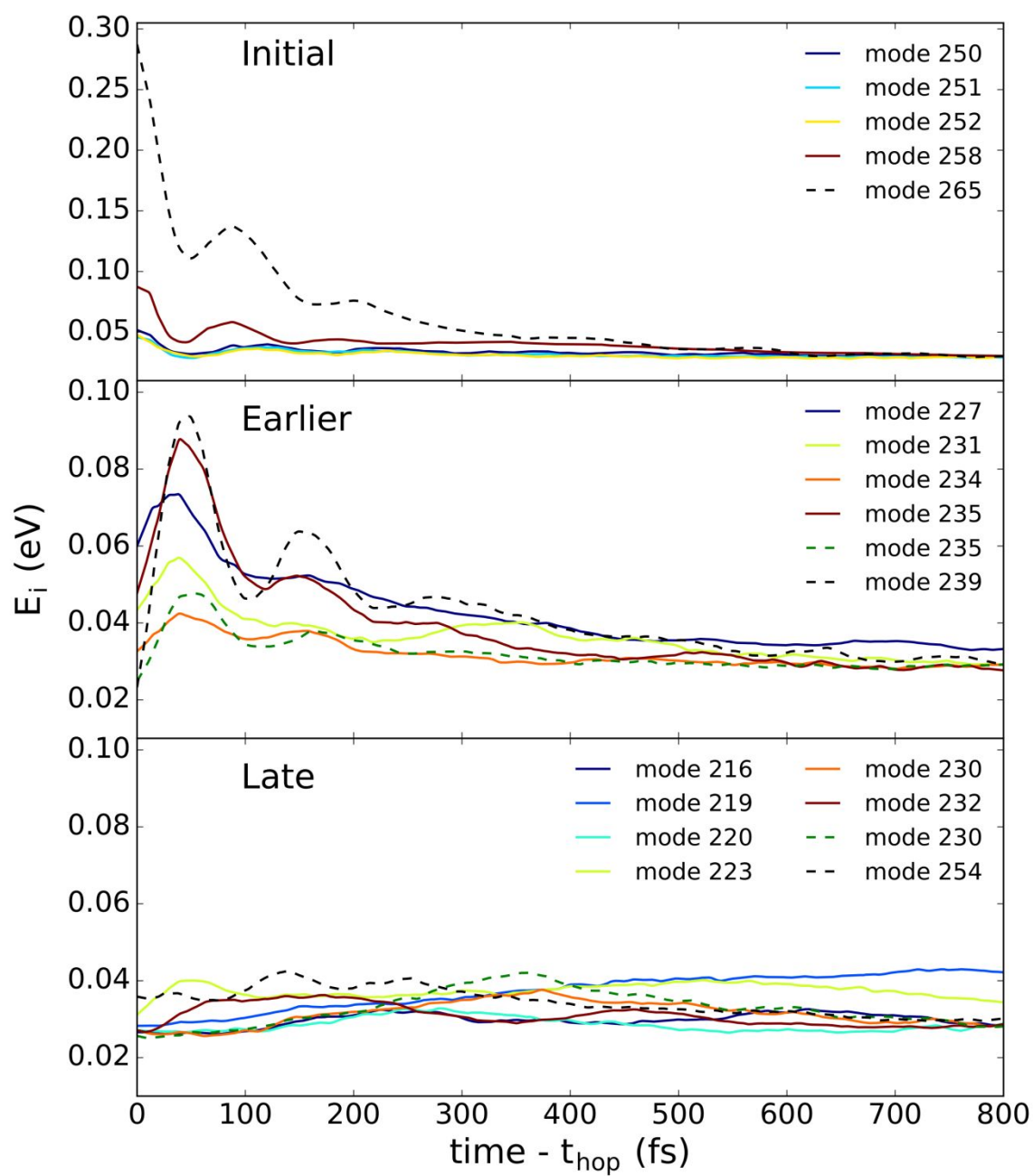


Figure 7

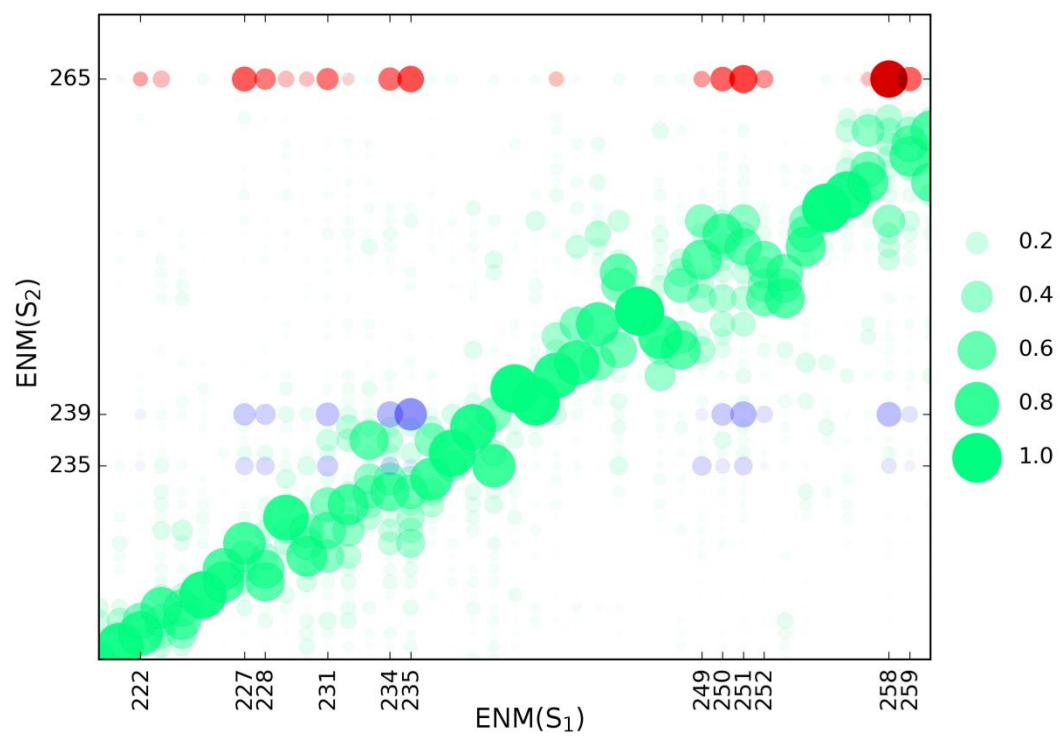
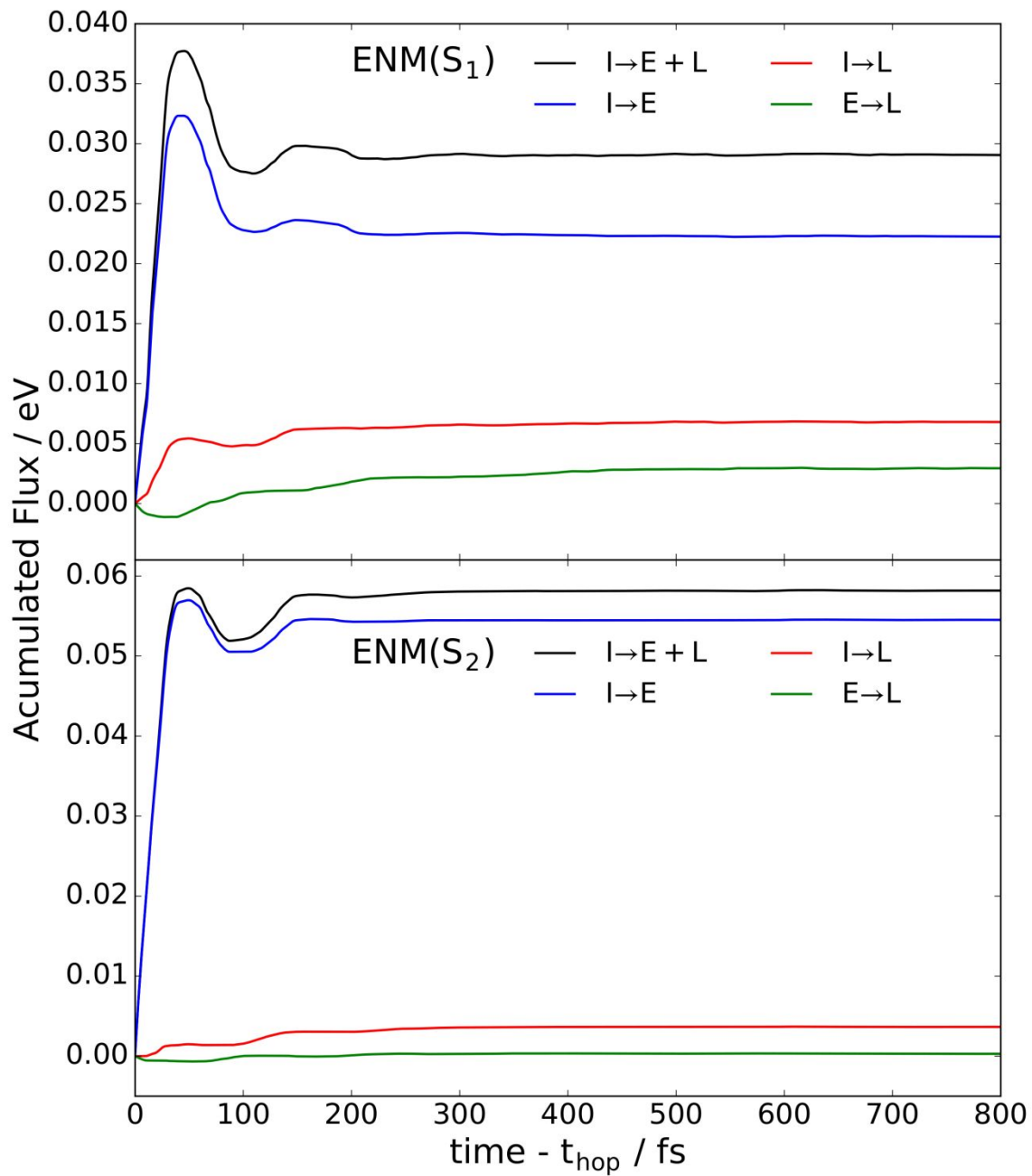
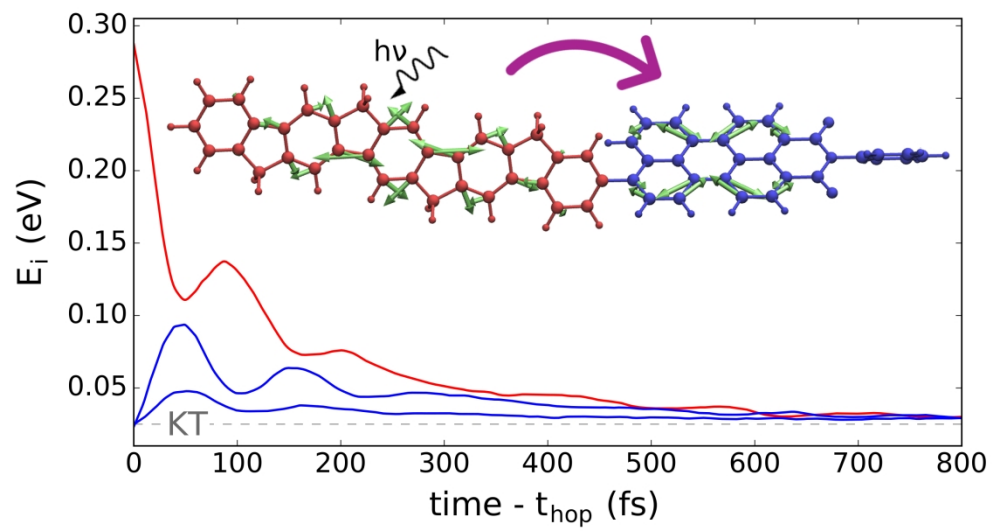


Figure 8





237x127mm (300 x 300 DPI)